Ceramics International 51 (2025) 16539–16550

Contents lists available at ScienceDirect

Ceramics International

journal homepage: www.elsevier.com/locate/ceramint

Spectroscopic, vibrational and structural insights into $LaYbO_3:Pr^{3+}$ and $LaLuO_3:Pr^{3+},Tb^{3+}$ perovskites at ambient and high-pressure conditions

M.T. Candela [a,c], F. Aguado [b,c,*], V. Monteseguro [b], J.A. González [b,c], R. Valiente [a,c]

[a] Departamento de Física Aplicada, Universidad de Cantabria, Avda. Los Castros 48, 39005, Santander, Spain
[b] Departamento CITIMAC, Universidad de Cantabria, Avda. Los Castros 48, 39005, Santander, Spain
[c] Grupo de Nanomedicina, IDIVAL-UC, Avda. Cardenal Herrera Oria, 39011, Santander, Spain

ARTICLE INFO

Handling Editor: Dr P. Vincenzini

Keywords:
Interlanthanide perovskites
Spectroscopy
Photoluminescence
High-pressure

ABSTRACT

The interlanthanide perovskites $LaYbO_3:Pr^{3+}$ and $LaLuO_3:Pr^{3+},Tb^{3+}$ were synthesized by a solid-state reaction and characterized at ambient conditions by means of X-ray diffraction (XRD), Raman spectroscopy and photoluminescence techniques. XRD measurements have shown that the synthesis method provided samples with pure perovskite phase (space group *Pnma*) for $LaYbO_3$, while in the case of the $LaLuO_3$ compound small traces of Lu_2O_3 could be found after several annealing. Up to 13 Raman active modes were observed in the Raman spectra of the studied perovskites and theoretical calculations performed for $LaYbO_3$ allowed to assign their symmetry. Regarding their optical properties, the emission from Tb^{3+} ions at *B* sites of the ABO_3 perovskite could be distinguished. Moreover, NIR emission from Pr^{3+} was observed in the $LaLuO_3$ perovskite at ~1000 nm and 1250–1600 nm. Emission in these spectral regions could be relevant for Si-based solar cell applications and fiber optic amplifiers, respectively. Moreover, the stability of both perovskites under high-pressure conditions has been studied spectroscopically, finding that $LaYbO_3$ is stable up to 19 GPa and that $LaLuO_3$ undergoes a possible pressure-induced phase transition at ~21–24 GPa. This makes $LaLuO_3$ the first interlanthanide perovskite showing phase transition under 40 GPa.

1. Introduction

It is known that binary rare-earth (RE) oxides with stoichiometry RE_2O_3 (typically denoted as rare-earth sesquioxides) can crystallize in three different structural conformations at ambient conditions: A (trigonal, *P-3m1*), B (monoclinic, *C2/m*) and C (cubic, *Ia-3*), being the stable phase dependent on the ionic radii of the RE ion and on thermal treatments [1]. Mixing RE' ions on a RE_2O_3 lattice can lead to the formation of $(RE_{1-x}RE'_x)_2O_3$ solid solutions with modified properties with respect to the pure compound. So far, several $(RE_{1-x}RE'_x)_2O_3$ series have been spectroscopically and/or structurally characterized at ambient conditions, including $(Eu_{1-x}Ho_x)_2O_3$ [2], $(Eu_{1-x}La_x)_2O_3$ [3], $(Eu_{1-x}Yb_x)_2O_3$ [4,5], $(Gd_{1-x}Yb_x)_2O_3$ [6], $(Gd_{1-x}Ho_x)_2O_3$ [6], $(Dy_{1-x}Ho_x)_2O_3$ [7], or $(Dy_{1-x}Er_x)_2O_3$ [8]. If RE and RE' ions are at (or near) equimolar proportions ($x = 0.5$), and if the size difference between them is large enough, ternary oxides with ABO_3 (*A* = RE, *B* = RE') perovskite-type structure can be formed. This type of compound, where both *A* and *B* are RE ions, is usually referred to as interlanthanide perovskites and they are an important family of materials that have been investigated for several applications: scintillators, protonic conductors or high-*k* materials, as well as for their magnetic properties [9–15]. However, despite their promising properties, they have been barely studied if compared with pure or doped RE_2O_3 with A-, B- and C-type structures, although there has been an increasing interest in them in the last decade [11]. Interlanthanide perovskite compounds were first reported in 1960 by *Schneider* et al. [16], who described the formation of four lanthanum-based perovskites ($LaRE'O_3$, *RE'* = Er, Tm, Yb, Lu). Currently, more interlanthanide perovskites are known to form after thermal treatments at room pressure. Some examples are: $LaREO_3$ (*RE* = Y, Ho), $REScO_3$ (*RE* = La-Tm, Y), $CeREO_3$ (*RE* = Tm-Lu), and $PrREO_3$ (*RE* = Yb-Lu) perovskite series [11,17–21]. Moreover, additional RE-based perovskites, such as $ErScO_3$ or $NdLuO_3$, can be formed by a joint high-pressure and high-temperature synthesis procedure [22,23].

Interlanthanide perovskites do not crystallize in the ideal $CaTiO_3$ cubic perovskite structure (*Pm-3m* space group), but in the orthorhombic distorted structure (*Pnma* space group), since the size difference between RE and RE' ions is not large enough to stabilize the ideal structure. The orthorhombic unit cell parameters (*a*, *b*, *c*) are related to

* Corresponding author. Departamento CITIMAC, Universidad de Cantabria, Avda. Los Castros 48, 39005, Santander, Spain.
E-mail address: aguadof@unican.es (F. Aguado).

https://doi.org/10.1016/j.ceramint.2024.09.151
Received 14 July 2024; Received in revised form 9 September 2024; Accepted 12 September 2024
Available online 13 September 2024

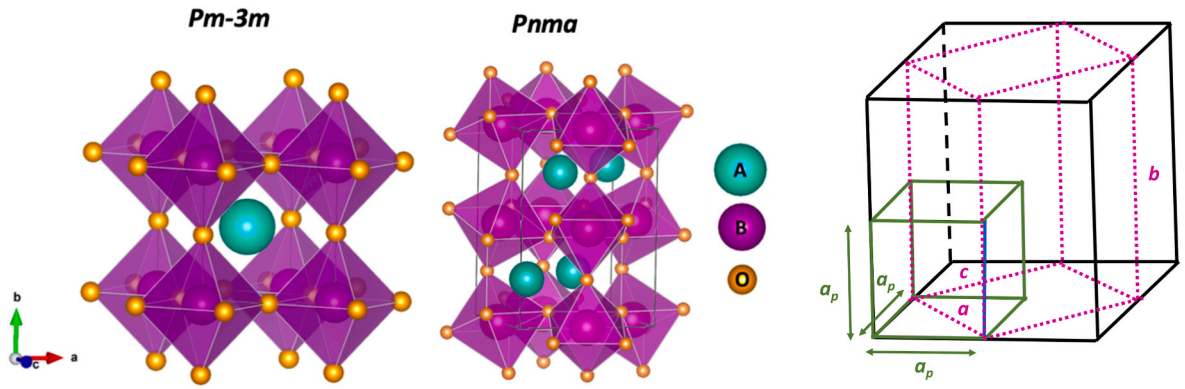

Fig. 1. View of the ideal (s.g. *Pm-3m*) and distorted (s.g. *Pnma*) ABO_3 perovskite along the indicated axes. The relationship between the lattice parameters of both structures is also depicted (right), where the pink dotted lines correspond to the orthorhombic structure and green solid lines to the cubic one (the black cube is just a guide). (For interpretation of the references to colour in this figure legend, the reader is referred to the Web version of this article.)

the cubic ones (a_p) by $a \approx c \approx \sqrt{2}a_p$ and $b = 2a_p$, also taking into account that the cubic axes are rotated by 45° around the *b* axis with respect to the orthorhombic form. A comparison between both structures is shown in Fig. 1.

In the *Pnma* structure, the distortion with respect to the ideal structure is caused by phase and antiphase rotations of the BO_6 octahedra (tilting), as can be observed in Fig. 1. Distortions from the ideal perovskite structure reduce the coordination number (CN) of the RE ion placed at the *A* site of the interlanthanide perovskite from 12 to 8 (AO_8 polyhedra). From the luminescent point of view, interlanthanide perovskites are excellent candidates to host optically active ions, since the emission intensity of the luminescent ion is enhanced when the site symmetry is lowered [24], as is the case of distorted perovskites. It is important to note that doping luminescent ions into a material's structure can enhance its properties and induce new ones, thus serving as a way of broadening their range of applications in several fields (e.g.: light-emitting devices, telecommunications, solar cells) [25–28].

If RE^{3+} ions are incorporated into an interlanthanide perovskite, they can substitute the RE ions placed at *A* or *B* sites of the host lattice, with C_s (CN = 8) and C_i (CN = 6) symmetries, respectively. It has been found that for several La-based interlanthanide perovskites doped with RE^{3+} ions (La*RE'*O_3:*RE''*, with *RE'* = Lu, Sc and *RE''* = Gd^{3+}, Tb^{3+}, Eu^{3+}), the fluorescence lifetime of RE^{3+} ions located at *B* sites is systematically larger than that of the ions placed at the *A* site. This behavior has been associated with the different site-symmetry of *A* and *B* sites, since the emission from optically active ions at the *B* site corresponds to forbidden transitions, as it is a centrosymmetric site [18,29]. Regarding La-based interlanthanide perovskites, it must be mentioned that they may have better luminescent efficiency than the doped La_2O_3:RE sesquioxide compound since La_2O_3 is quite unstable in air and it easily degrades into a mixture of $La(OH)_3$ and La_2O_3 with time, while RE-based perovskite-type oxides are referred to be more stable [30].

Interesting properties of perovskite materials, such as ferroelectricity or magnetism [31,32], are dependent on the structure and tilting distortions of the BO_6 octahedra, which can be modified by applying pressure or temperature. There are several studies on the high-pressure behavior of RE and transition-metal (M) perovskites (e.g.: RE*M*O_3, with *M* = Cr, Mn, Fe) [32–35], however, not all of them show the same structural evolution. For example, $LaCrO_3$ perovskite has been reported to reduce its distortion under compression, while in the case of *RE*CrO_3 (*RE* = Lu, Tb, Gd, Eu, Sm) series, the octahedral tilting is found to increase under the same conditions [32,33]. Meanwhile, research on the high-pressure behavior of interlanthanide perovskite oxides is scarce. In fact, and as far as we are concerned, only two interlanthanide perovskites have been studied (experimentally or theoretically) at high-pressure conditions so far: $CeScO_3$ [17,36] and $DyScO_3$ [37,38].

In this paper, we report the structural and spectroscopic characterization of $LaYbO_3$: Pr, and $LaLuO_3$: Pr,Tb interlanthanide perovskites at ambient conditions using X-ray diffraction (XRD), Raman spectroscopy and photoluminescence technique (PL). Density functional theory (DFT) calculations have been performed to assign the symmetry of $LaYbO_3$ vibrational modes observed in the Raman spectra. Furthermore, to shed light on the compression mechanism of the interlanthanide perovskite family, the stability of $LaYbO_3$:Pr and $LaLuO_3$:Pr, Tb up to a minimum of 19 GPa has been evaluated by spectroscopic techniques.

2. Experimental

2.1. Synthesis

Pr^{3+}-doped $LaYbO_3$ and Pr^{3+}- and Tb^{3+}-doped $LaLuO_3$ perovskites were synthesized by a solid-state reaction. The nominal compositions were $La(Yb_{1-x}Pr_x)O_3$ ($x = 0.005$) and $(La_{1-y}Pr_y)(Lu_{1-z}Tb_z)O_3$ ($y = 0.01$, $z = 0.001$). Hereafter, they will be named $LaYbO_3$:Pr and $LaLuO_3$:Pr,Tb, respectively. The synthesis procedure can be described as follows [39]: stoichiometric amounts of the corresponding starting RE_2O_3 were homogeneously mixed in an agate mortar for 15–20 min. After that, the mixed powders were pelletized in a hydraulic press (5 tons loading, 10 mm diameter pellet) and placed in an alumina crucible. The pellets were sintered in an air atmosphere at 1450 °C for 6–8 h and further ground until a fine powder was obtained. This process was repeated up to a maximum of four times in case the resulting powder had unreacted RE_2O_3.

2.2. Characterization

XRD powder patterns were measured in the 10°–110° 2θ range in a Bruker D8 Advanced diffractometer equipped with a Cu tube (λ = 1.5418 Å) and a fast Lynxeye-1D detector. Structural refinements (Rietveld) on the obtained XRD patterns were performed with TOPAS software [40]. The background function (modeled by a Chebychev polynomial), the zero error, the lattice parameters, the scale factor, the peak shape (Pseudo-Voigt), and the atomic positions were refined during the Rietveld refinement.

PL, excitation and lifetime measurements performed at room temperature (RT) were carried out in an FLS920 spectrofluorometer (Edinburg Inst.) equipped with double monochromators on emission and excitation arms, different excitation sources (a continuous 450 W Xe lamp, a 60 W pulsed lamp, a 4 W supercontinuum) and Hamamatsu R928P and H10330C photomultipliers (PTM) as detection systems.

Unpolarized RT Raman spectra were obtained with a T64000 Raman spectrometer (Horiba), equipped with a N_2-cooled CCD detector coupled to a confocal microscopy. Measurements were performed in subtractive

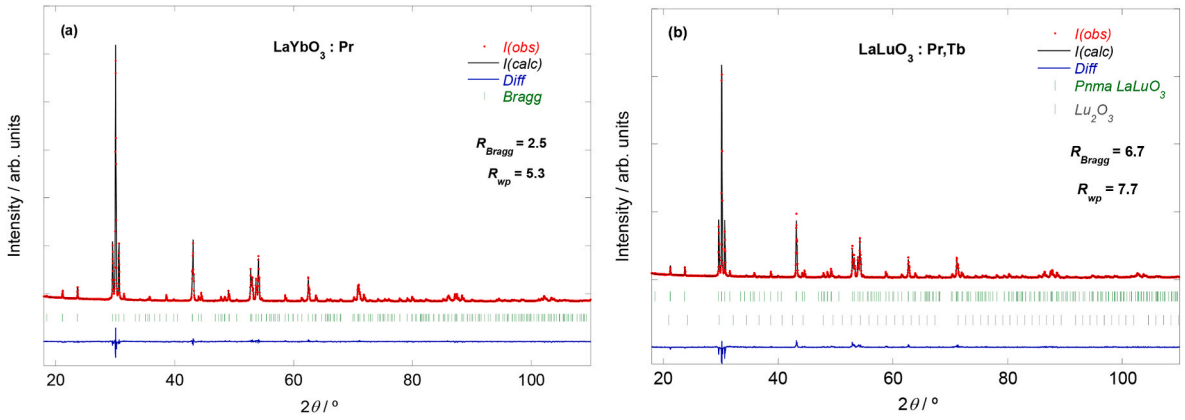

Fig. 2. Rietveld refinements of the RT XRD patterns of $LaYbO_3$:Pr (a) and $LaLuO_3$:Pr,Tb (b) perovskites, with their corresponding *R*-factors. Vertical lines correspond to Bragg reflections of the orthorhombic *Pnma* space group (a,b) and C-type Lu_2O_3 (b). Traces of Lu_2O_3 correspond to 1.5(2) %.

mode and the 514.5 or 488 nm laser lines of a Kr^+-Ar^+ laser were used as excitation sources in a backscattering configuration. The laser power on the sample was kept below 4 mW to minimize laser heating effects. High-pressure measurements were performed in a Boehler-Almax DAC, using ruby microspheres for pressure calibration and paraffin oil as a pressure-transmitting medium. High-pressure PL measurements were also carried out in the T64000 spectrometer with the 514.5 or 488 nm laser lines, depending on the sample.

3. Theoretical calculations

The Raman modes of $LaYbO_3$ perovskite were calculated theoretically. In order to assign the vibrational modes to their corresponding irreps, *ab-initio* total-energy calculations were performed within the framework of the density functional theory (DFT) [41]. The VASP package was used to carry out calculations with the pseudopotential method and the projector augmented wave scheme (PAW) [42]. We employ pseudopotentials, which replace the core electrons and make smoothed pseudo-valence wave functions. For lanthanum, 11 valence electrons are used ($5s^25p^65d^16s^2$), whereas 9 valence electrons ($4f^76s^2$) and 6 valence electrons ($2s^22p^4$) are used for ytterbium and oxygen, respectively. Highly converged results were achieved by extending the set of plane waves up to a kinetic energy cutoff of 450 eV. The exchange-correlation energy was taken in the generalized gradient approximation (GGA) with the PBEsol prescription [43]. A dense Monkhorst–Pack grid of *k*-special points (7 × 5 × 7) was used to perform integrations along the Brillouin zone (BZ) to obtain well-converged energies and forces. The structure was fully relaxed to its equilibrium configuration through the calculation of the forces on atoms and the stress tensor. In the relaxed configuration, the forces on the atoms are less than 0.006 eV/Å, and deviations of the stress tensor from a diagonal hydrostatic form are less than 0.1 GPa. Lattice-dynamics calculations were performed at the zone center (Γ point) of the BZ creating a supercell 2 × 2 × 2. Highly converged results on forces are required for the calculation of the dynamical matrix using the direct force constant approach [44,45]. The construction of the dynamical matrix at the Γ point of the BZ involves separate calculations of the forces in which a fixed displacement from the equilibrium configuration of the atoms within the primitive cell is considered. The number of such independent displacements in the analyzed structures is reduced due to the crystal symmetry. The software used to determine frequencies of the normal modes from the diagonalization of the dynamical matrix is Phonopy [44,45]. Moreover, these calculations allow identifying the symmetry, eigenvectors and eigenvalues of the vibrational modes in each structure at the Γ point.

4. Results and discussion

4.1. Characterization at ambient conditions

The XRD patterns of $LaYbO_3$:Pr and $LaLuO_3$:Pr,Tb compounds, synthesized by a solid-state reaction, are shown in Fig. 2. Both patterns

Table 1
Lattice parameters of $LaYbO_3$:Pr and $LaLuO_3$:Pr,Tb perovskites synthesized by a solid-state reaction. The *(θ, φ, Φ)* tilt angles calculated by Eq. (1) are also shown, together with the Goldschmidt tolerance factor (*t*) obtained from Eq. (2). Those of $LaLuO_3$:Tb(0.1 %) are included for comparison purposes. Lattice parameters from the rest of the compounds belonging to the $LaREO_3$ and $REScO_3$ series not studied in this work were taken from the indicated references.

Compound	*a*/Å	*b*/Å	*c*/Å	*θ*/°	*φ*/°	*Φ*/°	*t*	*ref*
$LaLuO_3$:Pr,Tb	6.0221(1)	8.3782(1)	5.8222(1)	14.8	10.7	18.2	0.863	This work
$LaLuO_3$:Tb	6.0262(1)	8.3834(1)	5.8265(1)	14.8	10.6	18.1	0.863	This work
$LaYbO_3$:Pr	6.0349(1)	8.4109(1)	5.8341(1)	14.8	11.2	18.6	0.860	This work
$LaHoO_3$	6.094	8.499	5.882	15.2	11.8	19.1	0.848	[52]
$LaYO_3$	6.100	8.512	5.889	15.1	12.0	19.2	0.849	[49]
$LaErO_3$	6.073	8.462	5.862	15.1	11.5	18.9	0.852	[24]
$LaTmO_3$	6.057	8.436	5.858	14.7	10.9	18.3	0.856	[49]
$YScO_3$	5.709	7.893	5.427	18.1	13.5	22.4	0.867	[53]
$HoScO_3$	5.715	7.901	5.429	18.2	13.6	22.6	0.867	[21]
$DyScO_3$	5.726	7.913	5.449	17.9	13.1	22.1	0.870	[21]
$TbScO_3$	5.729	7.917	5.465	17.5	12.5	21.4	0.874	[21]
$GdScO_3$	5.750	7.934	5.486	17.4	12.1	21.1	5.750	[21]
$EuScO_3$	5.755	7.949	5.509	16.8	11.5	20.3	0.883	[54]
$PrScO_3$	5.774	8.024	5.608	13.8	8.68	16.2	0.897	[55]
$CeScO_3$	5.777	8.045	5.642	12.4	7.34	14.4	0.903	[17]
$LaScO_3$	5.791	8.094	5.679	11.3	7.13	13.3	0.910	[56]

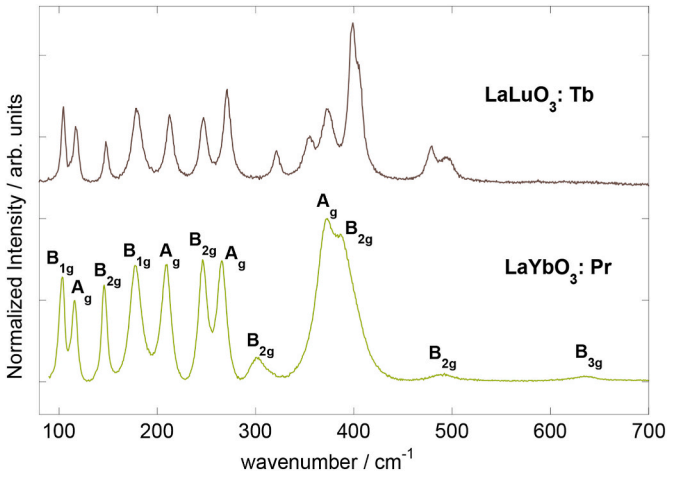

Fig. 3. RT Raman spectra of $LaYbO_3$:Pr and $LaLuO_3$:Tb perovskites recorded under 514.4 nm excitation.

could be indexed with the orthorhombic *Pnma* perovskite phase, although in the case of $LaLuO_3$:Pr,Tb compound small traces (1.5(2) %) of unreacted cubic (*Ia-3*) Lu_2O_3 were also found even after annealing the sample at 1450 °C during 6 or 8 h up to four times, as derived from Rietveld refinements (note that the detection limit of impurity phases with this technique is about is 4–5% or lower, and in cases with well-defined peaks, such as this, it can be 1–2%).

The unit cell parameters of $LaYbO_3$:Pr and $LaLuO_3$:Pr,Tb perovskites are collected in Table 1. They are in very good agreement with those previously reported for the pure compounds [9]. Thus, the small doping concentration of Pr^{3+} in $LaYbO_3$ (0.5%) or Pr^{3+} and Tb^{3+} in $LaLuO_3$ (1% and 0.1%, respectively) does not produce noticeable changes in the lattice parameters. It is worth mentioning that due to the large pseudocubic lattice parameter of $LaLuO_3$ ($a_{pc} \sim 4.18$ Å) and the possibility of being grown as a single crystal, some researchers have explored the possibility of synthesizing $(LaLuO_3)_{1-x}(LaScO_3)_x$ single crystals to address the lack of substrates with a_{pc} above 4 Å for the epitaxial growth of high-quality thin films [46]. The crystal structure of the perovskites studied in the present work is composed of a network of LaO_8 polyhedra linked to REO_6 slightly deformed octahedra. The bond distances (derived from the refined structure, see Tables S1 and S2 in *Supplementary Information* for atomic positions) vary as 2.29–2.97 Å and 2.34–3.03 Å in $LaLuO_3$ and $LaYbO_3$ LaO_8 polyhedra, respectively, and as 2.20–2.25 Å and 2.22–2.26 Å for REO_6 polyhedra, correspondingly (see detailed information in Table S3). As previously stated, the structural distortions in interlanthanide perovskites are manifested by in-phase and anti-phase rotations of the REO_6 octahedra. According to *Y. Zhao et al.*, this tilting can be described through three different angles (θ, φ, Φ) [47], being two of them (θ and φ) independent of each other. The angles θ and φ represent the rotations of the octahedra about the pseudo-cubic $[101]_p$ and $[010]_p$ axes, respectively (where pseudo-cubic axes refer to those of the ideal cubic perovskite) [48]. The angle θ can also be viewed as a single anti-phase tilt about the *a*-axis of the *Pnma* cell, while the φ angle is equivalent to an in-phase tilt about the *b*-axis [47]. The θ and φ angles can be combined into a single tilt angle Φ, which can be viewed as a rotation about the $[111]_p$ axis [48]. The three aforementioned tilting angles of the *Pnma* perovskite structure can be estimated from the lattice parameters through Eq. (1) [49] (assuming regular octahedra as an approximation) and their values are also collected in Table 1.

$$\theta = \cos^{-1}\left(\frac{c}{a}\right);\ \varphi = \cos^{-1}\left(\frac{\sqrt{2}c}{b}\right);\ \Phi = \cos^{-1}\left(\frac{\sqrt{2}c^2}{ab}\right) \quad (1)$$

The calculated tilt angles are slightly larger in $LaYbO_3$ than in $LaLuO_3$ (see Table 1), which is consistent with a smaller size difference between La and Yb ions, resulting in a larger distortion of the perovskite structure and thus in a lower Goldschmidt tolerance factor (*t*), which is a geometric factor used to predict the structural stability and the degree of distortion of perovskites and is defined as [50]:

$$t = \frac{R_A + R_O}{\sqrt{2}\,(R_B + R_O)} \quad (2)$$

where R_A, R_B, and R_O represent the ionic radii of *A*, *B*, and O ions. This factor usually takes the value $t \approx 1$ for the ideal cubic structure and 0.75–0.9 for distorted (tilted) ones [51], the latter being the case of the studied interlanthanide perovskites (see Table 1). The obtained tilt angles are larger than those calculated for other orthorhombic ABO_3 perovskites (with *A* and *B* either metal or RE ions) such as $CaTiO_3$ ($\theta = 8.9°$, $\varphi = 5.5°$, $\Phi = 10.4°$), $CdTiO_3$ ($\theta = 12.1°$, $\varphi = 10.0°$, $\Phi = 15.6°$) or $YAlO_3$ ($\theta = 13.6°$, $\varphi = 6.6°$, $\Phi = 15.1°$), with tolerance factors 0.959, 0.956 and 0.961, respectively, thus indicating a general larger structural distortion in the interlanthanide perovskites. This trend seems to be also true for other $LaREO_3$ perovskites and most of the $REScO_3$ ones, as summarized in Table 1 (see also S4 in *Supplementary Information*).

Fig. 3 shows the Raman spectra of the studied interlanthanide perovskites. Note that in the case of the $LaLuO_3$ compound, the Raman spectrum corresponds to that of $LaLuO_3$:Tb and not to that of $LaLuO_3$:Pr, Tb, to avoid interference of the strong luminescence of the Pr^{3+} ions in that perovskite with the Raman signal. According to group theory, up to 24 Raman modes are predicted for orthorhombic perovskites with *Pnma* space group ($\Gamma_{Pnma} = 7A_g + 5B_{1g} + 7B_{2g} + 5B_{3g}$) [38]. In our case, up to a maximum of 14 vibrational modes were experimentally detected for the synthesized perovskites. The smaller number of observed modes with respect to the expected ones could be the result of several factors, including the overlapping of nearby Raman modes or the low intensity due to the small polarizability of some vibrations. To assign the vibrational modes to their corresponding symmetry, the Raman modes of

Table 2
Assignment and experimental frequencies (ω_{exp}) of $LaYbO_3$:Pr and $LaLuO_3$:Tb Raman active modes at RT, compared with those previously reported for pure $LaYbO_3$ and $LaLuO_3$. In the case of $LaYbO_3$, the calculated frequencies (ω_{calc}) are also shown.

Symmetry	ω_{calc}/ cm^{-1} ($LaYbO_3$)	ω_{exp}[a]/ cm^{-1} ($LaYbO_3$:Pr)	ω_{exp}[b]/ cm^{-1} ($LaYbO_3$)	ω_{exp}[a]/ cm^{-1} ($LaLuO_3$:Tb)	ω_{exp}[c]/ cm^{-1} ($LaLuO_3$)
B_{3g}	95.83	–	–	–	–
B_{1g}	103.64	103.2(1)	104.5	104.9(1)	–
A_g	105.50	–	–	–	–
B_{2g}	114.03	–	–	–	–
A_g	114.37	115.9(1)	117.0	117.9(1)	122.5
B_{2g}	154.94	146.2(1)	147.2	148.5(1)	148.6
B_{1g}	168.68	178.3(1)	178.1	179.7(1)	183.0
A_g	208.53	209.0(1)	209.7	213.2(1)	214.8
B_{2g}	244.44	246.7(1)	246.8	247.4(1)	247.9
B_{3g}	249.67	–	–	–	–
A_g	276.20	265.5(1)	266.1	271.7(1)	270.8
B_{2g}	318.15	302.2(6)	301.0	321.8(1)	322.3
B_{1g}	355.14	–	–	354.6(1)	355.9
A_g	377.73	371.4(3)	369.8	373.9(1)	374.4
B_{3g}	389.02	–	–	–	–
B_{2g}	390.77	390.8(4)	390.4	398.9(1)	401.8
A_g	408.27	–	–	406.4(1)	–
B_{3g}	470.41	–	–	–	–
B_{2g}	487.13	492(2)	490.5	479.3(1)	482.0
B_{1g}	499.01	–	–	495.5(3)	494.0
A_g	509.71	–	–	–	–
B_{1g}	563.01	–	–	–	540.1
B_{2g}	615.56	–	–	–	–
B_{3g}	615.80	634(3)	649.2	–	–

[a] This work.
[b] Ref [57].
[c] Estimated from ref [14].

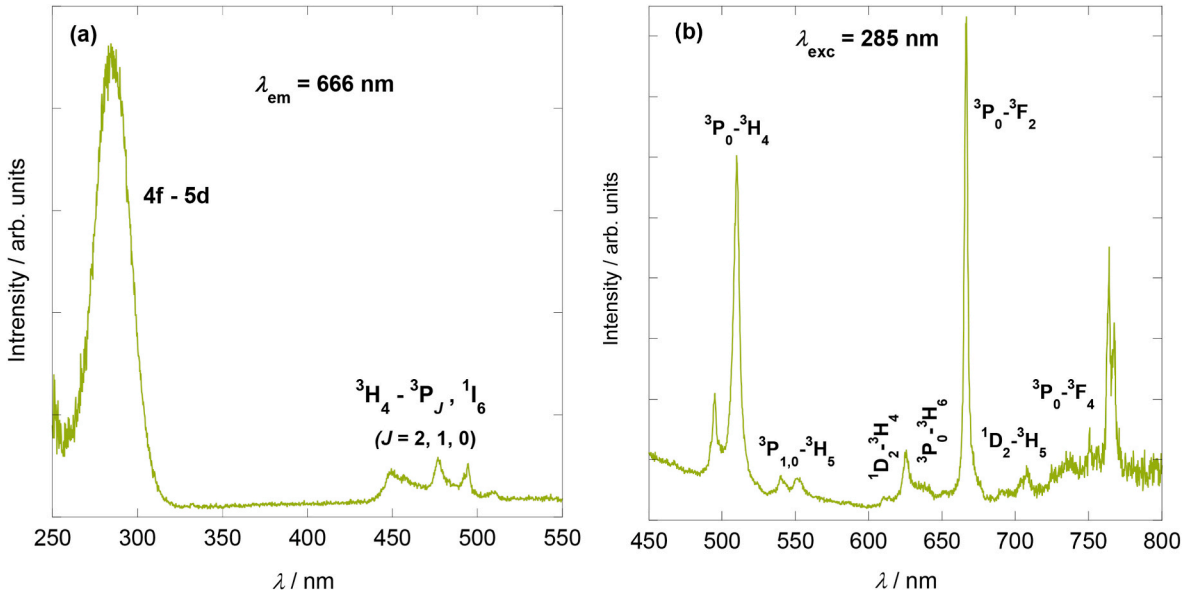

Fig. 4. RT excitation (a) and emission (b) spectra of Pr^{3+}-doped in $LaYbO_3$ perovskite.

$LaYbO_3$ were theoretically calculated according to a *Pnma* space group. Table 2 shows the calculated and experimental Raman modes of $LaYbO_3$, as well as those measured for $LaLuO_3$. The symmetry of the observed Raman modes of the latter compound was assigned based on the calculations performed for $LaYbO_3$. There is a fairly good agreement between the experimental frequencies and the calculated ones for most of the Raman modes of $LaYbO_3$ (Table 2). Also, the experimental frequencies are comparable to those previously reported for the pure perovskites [14,57].

In the case of the isostructural $CeScO_3$ and $DyScO_3$ perovskites, and according to phonon density of states (PDOS) calculations, the low-frequency Raman modes (<200 cm^{-1}) were reported to be mainly due to the motion of Ce^{3+} or Dy^{3+} ions, respectively, while those modes in the 200-400 cm^{-1} frequency range were reported to have more contributions from the Sc^{3+} cations. Moreover, the high-frequency modes were ascribed to oxygen anions, more specifically to internal vibrations of the ScO_6 octahedra (stretching vibrations) [36,38]. By inspection of Fig. 3 and Table 2, it can be observed that the low-frequency Raman modes (<250 cm^{-1}) barely change by modifying the atom at the *B* site of the perovskite (Lu, Yb). By analogy with $CeScO_3$ and $DyScO_3$ perovskites, it may be inferred that these modes are mainly due to La^{3+} motions. However, at higher frequencies, the Raman modes present changes depending on the RE ion that is part of the La*RE*O_3 perovskite (*RE* = Yb, Lu). It can be observed that the high-frequency modes of $LaLuO_3$:Pr,Tb are more blue-shifted if compared to those of $LaYbO_3$:Pr. This behavior would be in accordance with the fact that Lu^{3+} has a smaller ionic radius than Yb^{3+}, thus producing a shortening in the bond lengths and increasing the force constant (since $\omega \sim \sqrt{k}$), which would lead to a blueshift in the high-frequency Raman modes (and might correspond to stretching vibrations).

The study of the optical properties of $LaYbO_3$:Pr and $LaLuO_3$:Pr,Tb perovskites was performed by carrying out emission, excitation and fluorescence lifetime measurements. The RT excitation and emission spectra of Pr^{3+} ions in $LaYbO_3$:Pr are shown in Fig. 4. The excitation spectrum, measured recording the Pr^{3+} emission at 666 nm, consists of a broad band centered at 285 nm and a group of narrow peaks in the

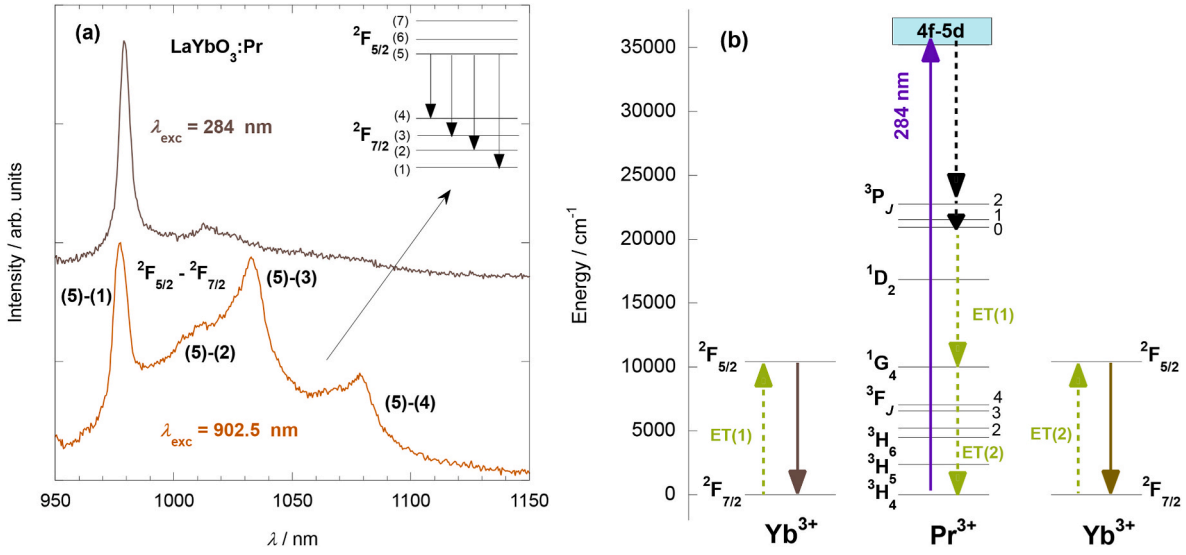

Fig. 5. (a) Emission spectra of Yb^{3+} in $LaYbO_3$:Pr perovskite under 284 and 902 nm excitation. The energy splitting of $^2F_{5/2}$ and $^2F_{7/2}$ levels drawn in the inset is arbitrarily assigned. (b) Energy diagram showing the possible energy transfer processes between Pr^{3+} and Yb^{3+} ions.

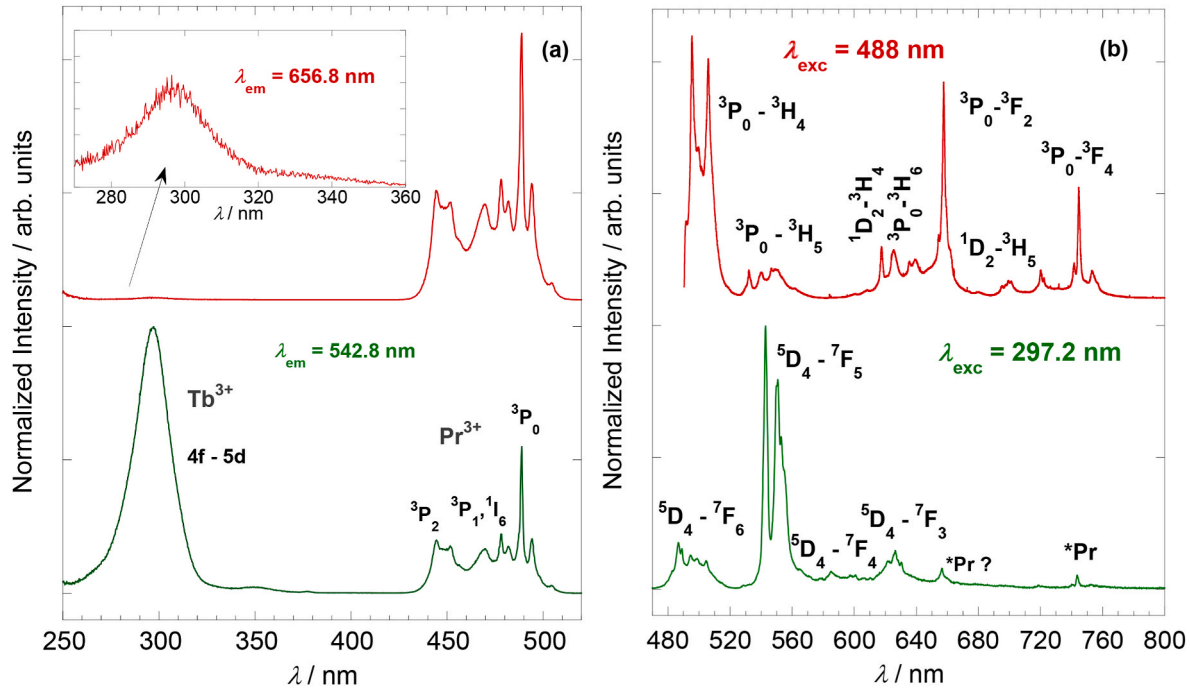

Fig. 6. Excitation spectra of $LaLuO_3$:Pr,Tb recording the emission at 656.8 nm and 542.8 nm (a) and emission spectra of the same compound recorded under 297.2 nm and 488 nm excitation (b). The emission spectrum in red (λ_{exc} = 488 nm) is mainly due to Pr^{3+} ions, while that in green (λ_{exc} = 297.2 nm) mainly corresponds to Tb^{3+} ions. (For interpretation of the references to colour in this figure legend, the reader is referred to the Web version of this article.)

430–530 nm range. These features are assigned to 4*f*-5*d* inter-configurational transitions and to $^3H_4 \rightarrow {}^3P_J$, $^1I_6$ intraconfigurational transitions of Pr^{3+} ions, respectively, as labeled in Fig. 4a. The emission spectrum was measured under 285 nm excitation and consists of sharp peaks mainly corresponding to transitions from ^3P_J excited states to the ^3H_J (J = 4–6) and ^3F_J (J = 2–4) low lying multiplets (Fig. 4b). Additionally, part of the ions in the $^3P_0$ excited state can further relax non-radiatively (*e.g.*, through multiphonon-relaxation or cross relaxations processes) to the $^1D_2$ level, from where emission can take place through $^1D_2 \rightarrow {}^3H_4$,$^3H_5$ transitions, as labeled in Fig. 4b. In the orthorhombic perovskite structure (*Pnma*), the dopant Pr^{3+} ions could be replacing La^{3+} ions, located at a non-centrosymmetric C_s site (CN = 8, R_{La} = 1.16 Å, $d_{La\text{-}O}$ = 2.33–3.03 Å) or substituting Yb^{3+} ions, placed at centrosymmetric C_i sites (CN = 6, R_{Yb} = 0.87 Å, $d_{Yb\text{-}O}$ = 2.22–2.25 Å), being both sites in a 1:1 ratio. The ionic radius of Pr^{3+} is closer to that of La^{3+} ($R_{Pr,CN=8}$ = 1.13 Å, $R_{Pr,CN=6}$ = 0.99 Å), thus substitution of La^{3+} by Pr^{3+} ions would be easier. However, the small number of peaks observable in the emission spectra could also be an indication that the Pr^{3+} ions are placed at a high-symmetry site, *i.e.*, replacing a Yb^{3+} ion in the octahedra, so this scenario cannot be discarded. In fact, since the starting RE_2O_3 were weighted during the synthesis procedure according to the ratios La^{3+}:Yb^{3+}:Pr^{3+} = 1:1-*x*:*x*, Pr^{3+} ions would in principle be incorporated into the *B*-site of the host lattice, although a small unintended anti-site doping could also take place, as reported for the site-selective doped $LaLuO_3$:Eu,Tb perovskite [29] and for $LaScO_3$:Tb,Gd [18]. The RT temporal evolution of the Pr^{3+} $^3P_0 \rightarrow {}^3F_2$ luminescence was measured by detecting the 667 nm emission after pulsed excitation at 477 nm. The decay curve could be fitted to a single exponential and the resultant PL lifetime was found to be τ = 0.38 μs.

Since Yb^{3+} ions are also luminescent, the emission spectrum of Yb^{3+} in $LaYbO_3$:Pr^{3+} perovskite was measured under 902 nm excitation, and it is shown in Fig. 5a. The NIR PL spectrum of Yb^{3+} consists of broad and asymmetric emission bands corresponding to transitions between the low energy Stark sublevels of the $^2F_{5/2}$ excited state and those of $^2F_{7/2}$ ground state. The observed bands located at around 977, 1010, 1033 and 1078 nm can thus be assigned to transitions between the Stark levels 5 → 1, 2, 3 and 4 (see energy levels in the inset of Fig. 5a).

Furthermore, it has been observed that upon 284 nm excitation, the wavelength at which Pr^{3+} ions are excited, NIR emission can be detected (Fig. 5a). This emission is different from that obtained after NIR excitation of Yb^{3+} ions at 902 nm, where the bands at 1033 and 1078 nm are hardly observed. Different interpretations can explain the NIR emission obtained after 284 nm excitation: i) it is indeed produced by the Pr^{3+} ions and it corresponds to luminescence originated by $^1D_2 \rightarrow {}^3F_{4,3}$ transitions, (which are also observed in $LaLuO_3$:Pr,Tb, as it will be discussed later), ii) it comes from Yb^{3+} and involves two subsequent energy transfer processes between Pr^{3+} and Yb^{3+} ions (see energy levels in Fig. 5b). The first energy transfer process implies a Pr^{3+} ion in the $^3P_0$ excited state and a Yb^{3+} ion in the $^2F_{7/2}$ ground state. The Pr^{3+} ion in the $^3P_0$ level decays non-radiatively to the $^1G_4$ state and transfers its energy to the Yb^{3+} ion in the ground state, which ends in the $^2F_{5/2}$ excited state and from which Yb^{3+} emission can take place. Moreover, the Pr^{3+} ion in the $^1G_4$ level, can decay non-radiatively to the $^3H_4$ ground state and transfer its energy to a second nearby Yb^{3+} ion in its ground state, which ends in the $^2F_{5/2}$ excited state, the level from which luminescence can be produced. iii) Another possible explanation is a quantum cutting mechanism, where a Pr^{3+} ion in the ^3P_J can transfer simultaneously its energy to two Yb^{3+} neighbor ions.

Fig. 6 shows the excitation (a) and luminescence (b) spectra of $LaLuO_3$:Pr,Tb perovskite at RT. The emission spectra were measured by exciting the sample at 297.2 nm with a Xe lamp and at 488 nm with a Kr^+-Ar^+ laser. By comparison of both PL spectra, it can be observed that the emission bands obtained under 297.2 and 488.8 nm excitation are different. The reason behind this behavior is that at 297.2 nm we are mainly exciting Tb^{3+} ions [29] ($^5D_4 \rightarrow {}^7F_J$ transitions, J = 3–6), while at 488 nm we are mainly exciting Pr^{3+} ions (^3P_J (J = 0,1) → ^3H_J (J = 4–6) and $^3P_0 \rightarrow {}^3F_J$ (J = 2–4) transitions), although PL features from Pr^{3+} ions can be found in the Tb^{3+} emission spectra (labeled in Fig. 6b with an asterisk), suggesting that there might be an energy transfer process between Tb^{3+} and Pr^{3+} ions (which is a possible process since Tb^{3+} $^5D_4$ and Pr^{3+} $^3P_0$ levels are energy resonant).

It is worth mentioning that it has been ruled out that the features

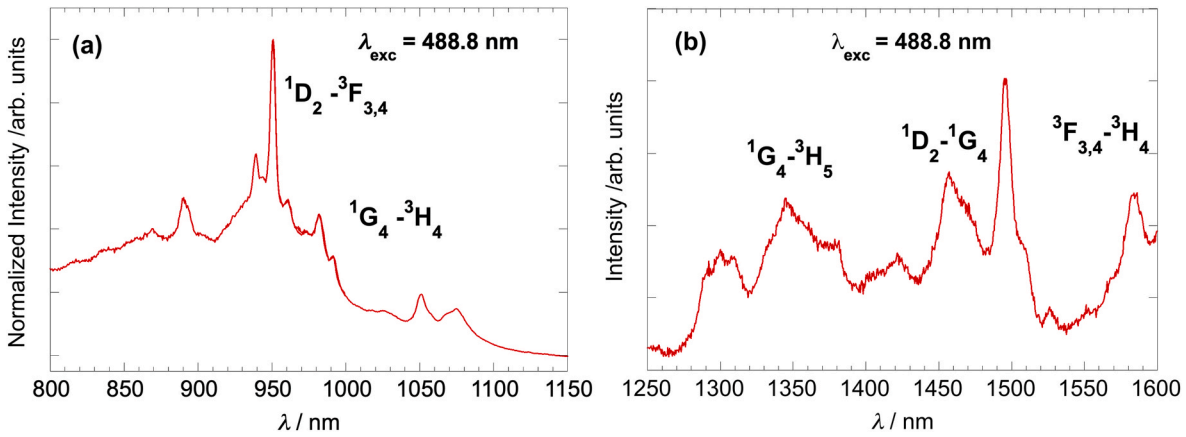

Fig. 7. NIR Pr^{3+} PL spectra of $LaLuO_3$:Pr,Tb with perovskite structure in the 800–1150 nm (a) and 1250–1600 nm (b) ranges under blue 488.8 nm excitation.

observed in the emission spectra belong to small traces of unreacted C-type Lu_2O_3:Tb present in the sample (which may have converted into Lu_2O_3:Tb,Pr by diffusion of Pr^{3+} ions during the solid state reaction), since they are fairly different from those previously reported for Tb^{3+} and Pr^{3+} ions in C_2 and S_6 sites of C-type Y_2O_3:Tb^{3+} and Y_2O_3:Pr^{3+}, respectively [58,59]. It must be remembered that the emission profile of RE^{3+} ions in different RE_2O_3 host lattices (or in any other host) will be similar as long as the symmetry around the RE ion is preserved, due to the effective shielding of the 4*f* electrons by the outer 5*s* and 5*p* ones [60]. Thus, the PL spectra of Tb^{3+} or Pr^{3+} in different C-type RE_2O_3 hosts will be fairly similar to those in the C-Lu_2O_3 host (as previously observed in Tb_2O_3 and Y_2O_3:Tb [58]). Thus, it can be concluded that the observed RE^{3+} emission comes indeed from those ions in the perovskite structure. Another fact that reinforces this statement is that the main emission band of $LaLuO_3$: Pr,Tb under 488 nm excitation is originated from the Pr^{3+} $^3P_0$ excited state, and transitions from this state are completely absent in Pr^{3+}-doped C-type sesquioxides [59,61].

Previous results on $LaLuO_3$ co-doped with Eu^{3+} and Tb^{3+} ions have reported the emission spectrum from Tb^{3+} in *A* and *B* sites of the *Pnma* ABO_3 perovskite by site-selective excitation [29]. In the mentioned studies, three excitation bands (at 200, 234 and 297 nm) were observed when detecting the Tb^{3+} emission at 545 nm. The band at 200 nm was attributed to host lattice excitations, while those bands at 234 and 297 nm were assigned to 4*f*-5*d* transitions from Tb^{3+} ions at *A* and *B* sites, respectively. Similar results were obtained in $LaScO_3$:Tb (1 %) perovskite (with slightly different excitation band positions) [18]. In our case, attempts to excite the sample at 234 nm yield almost no emission signal, thus, it can be concluded that the Tb^{3+} ions are mainly located at the centrosymmetric *B*-site. On the other hand, elucidating the site Pr^{3+} ions occupy in the $LaLuO_3$ host is not straightforward, as already mentioned in the case of $LaYbO_3$:Pr, although it is probable that they occupy the opposite site to that of the latter perovskite, since although both emission spectra resemble each other, the main Pr^{3+} emission bands are redshifted (~10 nm) in the case of $LaYbO_3$ host. Moreover, as the RE_2O_3 precursors were weighted during the synthesis procedure according to the ratios La^{3+}:Pr^{3+}:Lu^{3+}:Tb^{3+} = 1-*y*: *y*:1-*z*: *z*, Pr^{3+} ions should mainly occupy the *A* sites, while Tb^{3+} ions the *B* site. This hypothesis could be further reinforced by the fact that chemical pressure seems not to be the reason behind this shift, as the ionic radii of Lu^{3+} and Yb^{3+} for six-fold coordination are roughly the same (R_{Yb} = 0.868 Å, R_{Lu} = 0.861 Å). Also, the Pr^{3+} 4*f*-5*d* excitation band that was observable in $LaYbO_3$ is not detected in $LaLuO_3$ host.

It must be noticed that Pr^{3+} emission in the NIR 850–1150 nm and 1250–1600 nm ranges has also been detected in the studied perovskite upon 488.8 nm excitation (see Fig. 7) at RT. The emission bands in the 850–1150 nm can be assigned to $^1D_2 \rightarrow {}^3F_{4,3}$ and $^1G_4 \rightarrow {}^3H_4$, while those in the 1250–1600 nm range originate from $^1G_4 \rightarrow {}^3H_5$, $^1D_2 \rightarrow {}^1G_4$ and $^3F_{3,4} \rightarrow {}^3H_4$ Pr^{3+} transitions. It is worth mentioning that compounds

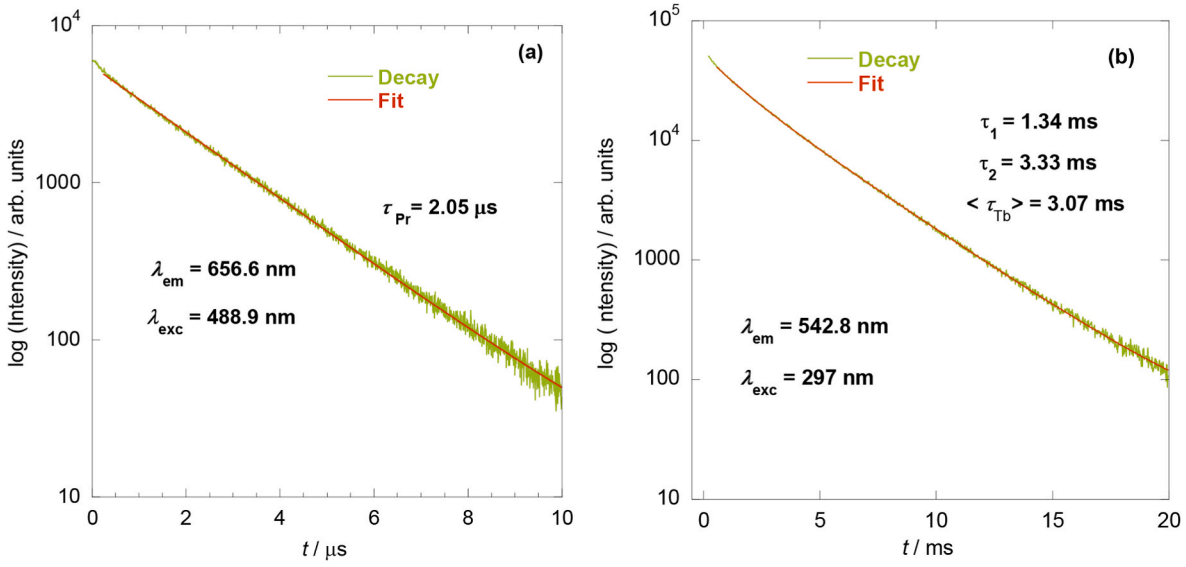

Fig. 8. Temporal evolution of the $^3P_0$ Pr^{3+} (a) and $^5D_4$ Tb^{3+}(b) luminescence in $LaLuO_3$:Pr,Tb perovskite.

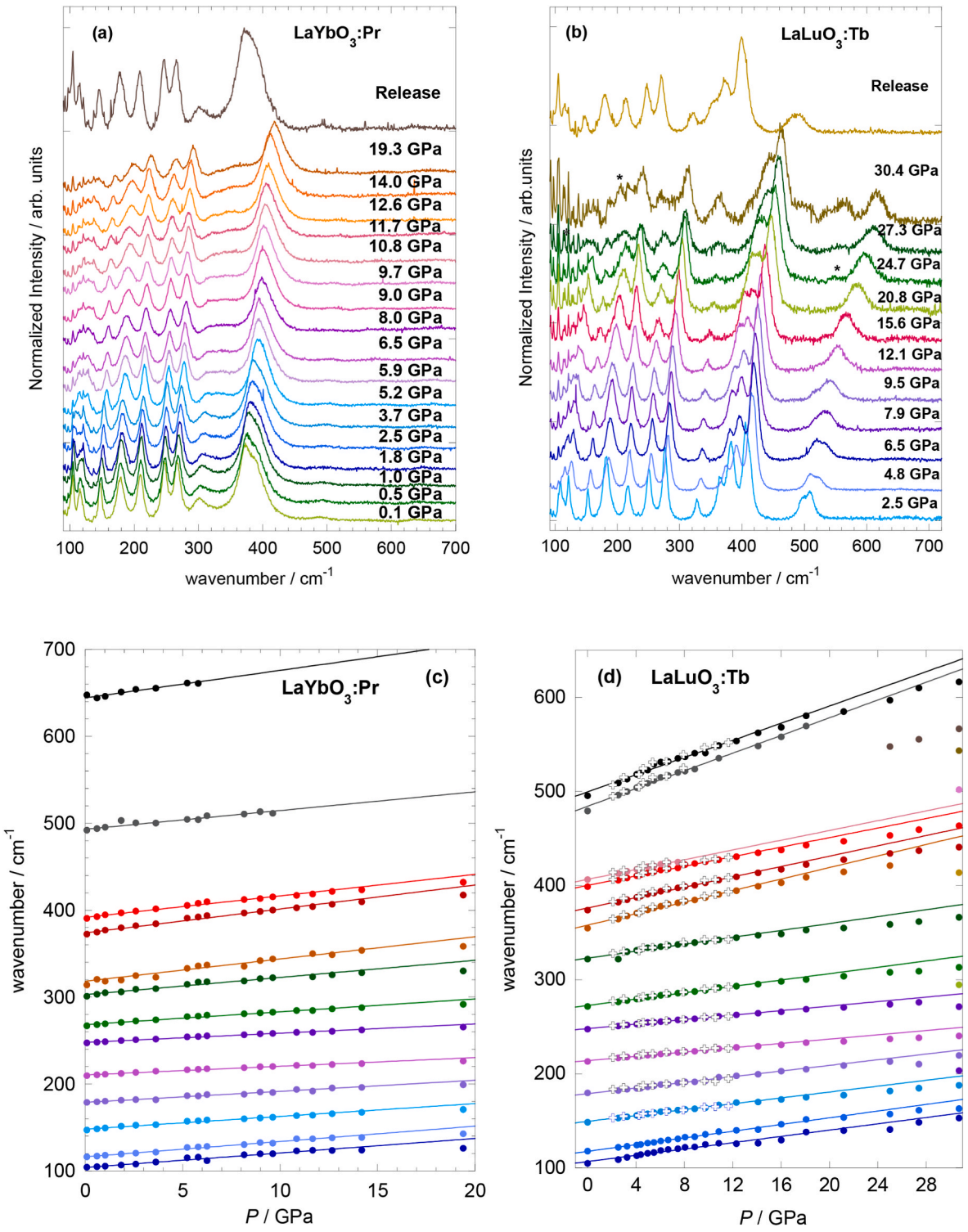

Fig. 9. Raman spectra of $LaYbO_3$:Pr and $LaLuO_3$:Tb perovskites as a function of pressure, together with the spectrum at pressure release (a, b) and pressure shift of their corresponding Raman modes (c, d). The fitting was performed with data in the 0–15 GPa range and the excitation wavelength was 514.5 nm.

with an intense Pr^{3+} NIR emission at ~1000 nm under UV–Vis excitation are interesting for photovoltaic applications since this region (950–1050 nm) corresponds to that at which the spectral response of Si-based solar cells is maximum [62]. Also, the Pr^{3+} NIR emission in the 1250–1600 nm range is located at the so-called *telecom window* and thus, compounds with emission bands located in this region are useful to be used as optical fiber amplifiers in the O-band (1260–1360 nm) and S-band (1460–1530 nm) [63–65].

The temporal evolution of Pr^{3+} and Tb^{3+} visible luminescence in $LaLuO_3$:Pr,Tb perovskite has been recorded by detecting the emission at 656.8 nm and 542.8 nm, respectively, after a pulsed excitation at 488.8 nm (Pr^{3+}) or 297 nm (Tb^{3+}). The decay curves of both ions are shown in Fig. 8 and they have been fitted to a single exponential in the case of the temporal evolution of Pr^{3+} ions (Fig. 8a) and to a double exponential in the case of Tb^{3+} ions (Fig. 8b). The average luminescence lifetime was $\tau = 2.05$ μs for Pr^{3+} ions and $\tau = 3.07$ ms for Tb^{3+} ions.

4.2. Behavior at high-pressure

The high-pressure behavior of $LaYbO_3$ and $LaLuO_3$ perovskites was studied by spectroscopic means through PL and/or Raman experiments. Fig. 9 shows representative high-pressure Raman spectra of $LaYbO_3$:Pr (a), $LaLuO_3$:Tb (b) perovskites measured under 514.5 nm excitation, as well as the pressure-shift of their corresponding Raman modes (c, d). Note that in this case Raman experiments were carried out again on a $LaLuO_3$:Tb sample, rather than on $LaLuO_3$:Pr,Tb one, to prevent interference of the luminescence from Pr^{3+} ions with the Raman signal. Due to the small amount of Pr^{3+} doping (1 %) in the latter perovskite, the high-pressure behavior is expected to be about the same in both perovskites.

As can be observed from Fig. 9, the overall appearance of the Raman spectra is maintained up to ~19 GPa in $LaYbO_3$:Pr and below 24 GPa in $LaLuO_3$:Tb, with no new peaks appearing in that pressure range. Only a broadening of the peaks with pressure (probably due to the solidification of paraffin oil) and a decrease in the relative intensities of some peaks (mainly visible for the low-frequency ones) are observed. The Raman modes shift towards higher frequencies with increasing pressure, indicating a strengthening and shortening in the RE-O bonds. Moreover, this shift is noticeable even for the lowest frequency vibrational modes, in contrast with what was previously found for binary RE_2O_3 with a C-type structure [58,66]. The shift of the Raman modes appears to be mostly linear in both perovskites up to ~15 GPa, while above that pressure, the frequency dependence generally tends to deviate from its initial linear trend (although in the case of $LaYbO_3$ it cannot be assured, since only one measurement was done for pressures higher than 15 GPa). The curvature in the frequency-pressure relationship beyond 15 GPa has also been predicted for $DyScO_3$ interlanthanide perovskite through theoretical calculations [38]. Table 3 shows the pressure derivatives ($\partial\omega_i/\partial P$) of the observed Raman modes for the two studied perovskites up to 15 GPa. In the case of $LaYbO_3$, the Grüneisen parameters (γ) were also estimated using Eq. (3). Since no experimental value of the bulk modulus (B_0) has been reported for this compound, the theoretical one has been used instead ($B_0 = 150$ GPa) [67].

$$\gamma = \left(\frac{B_0}{\omega_0}\right)\cdot\left(\frac{\partial\omega_i}{\partial P}\right) \tag{3}$$

From Tables 3 and it can be observed that the pressure derivatives are found to be similar (for equivalent Raman modes) in both perovskites and to be larger for the high-frequency modes. However, the Grüneisen parameters in $LaYbO_3$ do not seem to follow a clear trend. In fact, they are higher for the low-frequency modes. This behavior has been also observed in $CeScO_3$ perovskite [36].

High-pressure Raman measurements on $LaLuO_3$:Tb perovskite suggest that the orthorhombic phase is stable up to about ~ 24 GPa, a pressure at which a new mode around 550 cm^{-1} seems to emerge. At higher pressures, the new peak splits into two contributions and a new mode appears at ~ 200 cm^{-1} at 30 GPa. This suggests that a phase transition is taking place. However, XRD diffraction experiments at high pressure would be needed to elucidate the symmetry of the new phase. Meanwhile, in the case of $LaYbO_3$:Pr perovskite no phase transition was detected in the explored pressure range. The spectrum obtained after pressure release, also shown in Fig. 9, is the same as the one of the starting materials for both perovskites, indicating the eventual high-pressure phase transition in $LaLuO_3$:Tb is reversible.

The high-pressure behavior of $LaLuO_3$:Pr,Tb perovskite was also studied through Pr^{3+} luminescence since RE^{3+} ions luminescence can be used as a structural probe. The Pr^{3+} emission spectrum of $LaLuO_3$:Pr,Tb was recorded under 488 nm excitation and it is shown in Fig. 10a for selected pressures. The PL spectra are dominated by the $^3P_0 \rightarrow {}^3H_4$ and $^3P_0 \rightarrow {}^3F_2$ intraconfigurational transitions, which shift towards higher wavelengths upon increasing pressure, with pressure coefficients equal to 0.36 and 0.62 nm/GPa (0–18 GPa range) for the most intense peak, respectively (see Fig. 10b).

At 21.4 GPa there is an observable increase in the integrated intensity of the emission band located between 610 and 680 nm, which points out to a modification around the crystal environment of Pr^{3+} ions, compatible with the development of a new high-pressure phase. At 31 GPa, this band dominates the PL spectra and the emission from the $^3P_0 \rightarrow {}^3H_4$ is only residual. The emission spectrum was measured after pressure release and is also shown in Fig. 10a. It can be observed that the spectrum after decompression is identical to the one of the starting material, although with a slightly less resolved profile due to residual stress on the sample, indicating thus the reversibility of the pressure-induced phase transition, as previously suggested by Raman measurements.

As far as we are concerned, only $CeScO_3$ and $DyScO_3$ interlanthanide perovskites have been experimentally studied at high-pressure conditions so far and they have been found to be stable, showing no evidence of structural phase transitions in the 0–40 GPa pressure range [17,37]. It should be mentioned that in the case of $DyScO_3$, theoretical studies have predicted that above 60 GPa the orthorhombic structure becomes unstable and a possible phase transition towards the *Cmcm* post-perovskite phase has been proposed, since above 14.4 GPa this phase has a lower enthalpy than the *Pnma* one, although further studies would be needed

Table 3
Symmetry, ambient frequency (ω_0) and pressure derivatives ($\partial\omega_i/\partial P$) of the Raman active modes of the studied $LaYbO_3$:Pr and $LaLuO_3$:Tb perovskites belonging to the orthorhombic *Pnma* phase. Experimental parameters were derived from the fitting of the measured data (0–15 GPa) to a linear dependence $\left(\omega = \omega_0 + \left(\frac{\partial\omega_i}{\partial P}\right)P\right)$. Grüneisen parameters were also estimated for $LaYbO_3$. Standard deviations are shown in parentheses.

Mode	$LaYbO_3$:Pr			$LaLuO_3$:Tb	
	ω_0 (cm^{-1})	$\partial\omega_i/\partial P$ (cm^{-1}/GPa)	γ	ω_0 (cm^{-1})	$\partial\omega_i/\partial P$ (cm^{-1}/GPa)
B_{1g}	103.89(5)	1.67(1)	2.41(1)	106.7(9)	1.7(1)
A_g	116.1(7)	1.76(1)	2.27(2)	117.6(4)	1.78(5)
B_{2g}	147.82(4)	1.48(1)	1.50(1)	149.4(4)	1.56(5)
B_{1g}	178.80(6)	1.27(1)	1.07(8)	178.9(4)	1.50(4)
A_g	210.36(4)	1.00(1)	0.71(1)	214.0(2)	1.14(3)
B_{2g}	247.75(4)	1.06(1)	0.64(1)	248.0(2)	1.20(2)
A_g	268.17(5)	1.48(1)	0.83(1)	272.6(3)	1.69(4)
B_{2g}	302.9(3)	1.97(5)	0.97(2)	323(1)	1.8(1)
B_{1g}	–	–	–	358(8)	3.1(1)
A_g	373.8(1)	2.76(2)	1.10(1)	376.3(6)	2.75(7)
B_{2g}	391.7(2)	2.47(5)	0.94(2)	400.2(4)	2.55(6)
A_g	–	–	–	406.7(4)	2.59(7)
B_{3g}	–	–	–	–	–
B_{2g}	493.1(9)	2.2(2)	0.67(6)	484(1)	4.7(2)
B_{1g}	–	–	–	499(1)	4.6(2)
B_{3g}	644(2)	3.2(9)	0.7(2)	–	–

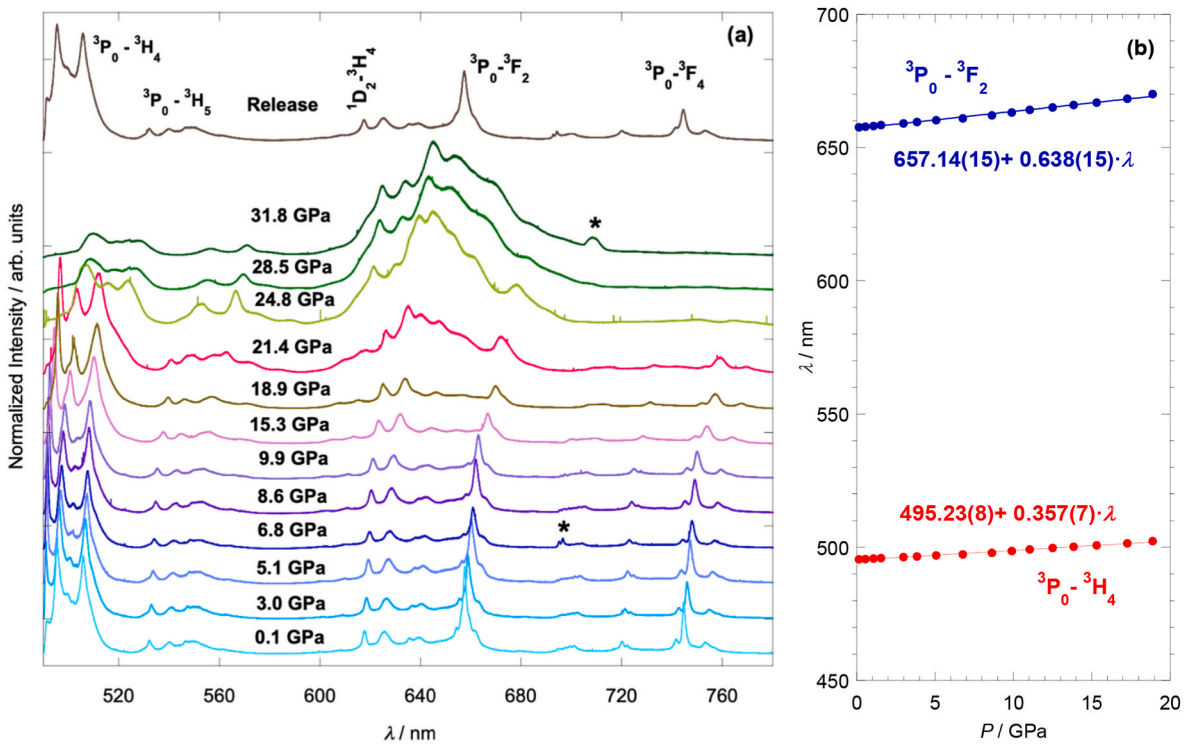

Fig. 10. (a) High-pressure PL spectra of Pr^{3+} in $LaLuO_3$ perovskite measured under 488 nm laser excitation. Peaks marked with an asterisk correspond to the ruby luminescence. (b) Pressure shift of the most intense peak of the $^3P_0 \rightarrow {}^3H_4$ and $^3P_0 \rightarrow {}^3F_2$ transitions.

to corroborate the hypothesis [38]. Thus, up to date, $LaLuO_3$:Pr,Tb is the only interlanthanide perovskite showing experimentally a pressure-induced phase transition well below 40 GPa. Lower stability of this compound could be related, however, to the smaller hydrostatic range of the employed pressure transmitting media (paraffin oil) if compared with those used in $DyScO_3$ (4:1 methanol-ethanol mixture) or $CeScO_3$ (16:3:1 methanol-ethanol-water).

5. Conclusions

Two lanthanum-based perovskites, $LaYbO_3$:Pr and $LaLuO_3$:Pr,Tb, were successfully synthesized by a solid-state reaction, as corroborated by XRD measurements, although in the case of $LaLuO_3$ the pure phase could not be isolated and small traces of Lu_2O_3 were found in all cases. Increasing the temperature ($T > 1500$ °C) during the sintering process might improve the possibility of achieving an impurity-free perovskite. The Raman frequencies of $LaYbO_3$ obtained from DFT calculations agree fairly well with those observed experimentally for Pr-doped $LaYbO_3$, which has allowed us to assign the symmetry of the observed vibrational modes in the two studied compounds. Our experimental frequencies match the ones reported in previous studies for the pure compounds. Photoluminescence measurements in $LaLuO_3$:Pr,Tb perovskite allowed us to observe NIR emission from Pr^{3+} ions in the 950–1150 nm and 1250–1600 nm ranges, which could be of interest for applications in the field of telecommunications or Si-based solar cells, although further research is needed. The emission from Tb^{3+} ions placed in the centrosymmetric *B* site of the perovskite has been distinguished. Moreover, emission from Pr^{3+} placed at *A* sites in $LaLuO_3$ and at *B* sites in $LaYbO_3$ has been inferred. Different interpretations have been given to the NIR emission observed in $LaYbO_3$:Pr under UV excitation, including energy transfer between Pr^{3+} and Yb^{3+} ions, quantum cutting and the emission of praseodymium itself. Lastly, the stability of the interlanthanide perovskites under high-pressure conditions has been studied by spectroscopic means. $LaYbO_3$:Pr perovskite was found to be stable in the explored pressure range (up to 19 GPa), while $LaLuO_3$:Pr,Tb undergoes a phase transition at about 21–24 GPa. Notably, $LaLuO_3$ is the first intra-rare-earth perovskite to exhibit a pressure-induced phase transition below 40 GPa. Future research using high-pressure XRD measurements will aim to determine whether the structure transitions to a higher or lower symmetry phase.

CRediT authorship contribution statement

M.T. Candela: Writing – original draft, Investigation. **F. Aguado:** Writing – review & editing, Supervision, Investigation, Formal analysis, Conceptualization. **V. Monteseguro:** Writing – review & editing, Investigation. **J.A. González:** Writing – review & editing, Investigation. **R. Valiente:** Writing – review & editing, Supervision, Funding acquisition, Conceptualization.

Acknowledgments

M.T.C. thanks the University of Cantabria and the Government of Cantabria for the pre-doctoral grant “Concepción Arenal”. V.M. acknowledges the “Beatriz Galindo” fellowship (BG20/000777). The authors thank the financial support from the European Union (FET Open project NCLas, ref. H2020-EU829161) and from MCIN/AEI/ 10.13039/501100011033 and the European Union (Grants PID2021–127656NB-I00 and PID2021-125927NA-C22).

Appendix A. Supplementary data

Supplementary data to this article can be found online at https://doi.org/10.1016/j.ceramint.2024.09.151.

References

[1] M. Zinkevich, Thermodynamics of rare earth sesquioxides, Prog. Mater. Sci. 52 (2007) 597–647, https://doi.org/10.1016/j.pmatsci.2006.09.002.

[2] K.A. Irshad, N.V. Chandra-Shekar, T.R. Ravindran, V. Srihari, K.K. Pandey, X-ray diffraction and Raman studies on Ho:Eu_2O_3, J. Mol. Struct. 1128 (2017) 325–329, https://doi.org/10.1016/j.molstruc.2016.08.077.

[3] K.A. Irshad, A. Saikumaran, V. Srihari, S. Kalavathi, N.V. Chandra Shekar, Microstrain-assisted polymorphic phase transitions in $(Eu_{1-x}La_x)_2O_3$, J. Appl. Crystallogr. 52 (2019) 32–39, https://doi.org/10.1107/S1600576718016989.

[4] M.T. Candela, F. Aguado, A. Diego-Rucabado, J.A. González, R. Valiente, Non-resonant energy transfer from Eu^{3+} to Yb^{3+} in C-type and B-type $(Eu_{1-x}Yb_x)_2O_3$ nanocrystals, J. Alloys Compd. 921 (2022) 166043, https://doi.org/10.1016/j.jallcom.2022.166043.

[5] Z.K. Heiba, Y. Akin, W. Sigmund, Y.S. Hascicek, X-ray structure and microstructure determination of the mixed sesquioxides $(Eu_{1-x}Yb_x)_2O_3$ prepared by a sol-gel process, J. Appl. Crystallogr. 36 (2003) 1411–1416, https://doi.org/10.1107/S0021889803019319.

[6] Z.K. Heiba, L. Arda, Y.S. Hascicek, Structure and microstructure characterization of the mixed sesquioxides $(Gd_{1-x}Yb_x)_2O_3$ and $(Gd_{1-x}Ho_x)_2O_3$ prepared by sol-gel process, J. Appl. Crystallogr. 38 (2005) 306–310, https://doi.org/10.1107/S0021889805000609.

[7] Z.K. Heiba, M. Bakr Mohamed, H. Fuess, XRD, IR, and Raman investigations of structural properties of $Dy_{2-x}Ho_xO_3$ prepared by sol gel procedure, Cryst. Res. Technol. 47 (2012) 535–540, https://doi.org/10.1002/crat.201200032.

[8] Z.K. Heiba, M. Bakr Mohamed, M.A. Abdelslam, L.H. Fuess, Structure, microstructure and magnetic properties of mixed rare earth oxide $(Dy_{1-x}Er_x)_2O_3$, Cryst. Res. Technol. 46 (2011) 272–276, https://doi.org/10.1002/crat.201000706.

[9] K. Ito, K. Tezuka, Y. Hinatsu, Preparation, magnetic susceptibility, and specific heat on interlanthanide perovskites ABO_3 (A=La-Nd, B=Dy-Lu), J. Solid State Chem. 157 (2001) 173–179, https://doi.org/10.1006/jssc.2000.9071.

[10] A. Martinelli, R. Masini, C. Artini, G.A. Costa, L. Keller, DC magnetic susceptibility and neutron powder diffraction analysis of the perovskite-type compounds $LaYbO_3$ and $LaHoO_3$, J. Phys. Condens. Matter 25 (2013) 426005, https://doi.org/10.1088/0953-8984/25/42/426005.

[11] C. Artini, Crystal chemistry, stability and properties of interlanthanide perovskites: a review, J. Eur. Ceram. Soc. 37 (2017) 427–440, https://doi.org/10.1016/j.jeurceramsoc.2016.08.041.

[12] A. Martinelli, C. Artini, L. Keller, New insights into the magnetic properties of $LaErO_3$, $(La_{0.5}Er_{0.5})_2O_3$ and $(La_{0.5}Dy_{0.5})_2O_3$ oxides, J. Phys. Condens. Matter 28 (2016) 066003, https://doi.org/10.1088/0953-8984/28/6/066003.

[13] Y. Larring, T. Norby, Protons in $LaErO_3$, Solid State Ionics 70–71 (1994) 305–310, https://doi.org/10.1016/0167-2738(94)90327-1.

[14] J. Varghese, T. Joseph, M.T. Sebastian, N. Reeves-McLaren, A. Feteira, Crystal structure and microwave dielectric properties of LaLuO3 ceramics, J. Am. Ceram. Soc. 93 (2010) 2960–2963, https://doi.org/10.1111/j.1551-2916.2010.03930.x.

[15] S. Coh, T. Heeg, J.H. Haeni, M.D. Biegalski, J. Lettieri, L.F. Edge, K.E. O'Brien, M. Bernhagen, P. Reiche, R. Uecker, S. Trolier-Mckinstry, D.G. Schlom, D. Vanderbilt, Si-compatible candidates for high-κ dielectrics with the *Pbnm* perovskite structure, Phys. Rev. B Condens. Matter 82 (2010) 064101, https://doi.org/10.1103/PhysRevB.82.064101.

[16] S.J. Schneider, R.S. Roth, Perovskite-type compounds in binary rare earth oxide systems, J. Am. Ceram. Soc. 43 (1960) 115, https://doi.org/10.1111/j.1151-2916.1960.tb13650.x, 115.

[17] D. Errandonea, D. Santamaria-Perez, D. Martinez-Garcia, O. Gomis, R. Shukla, S. N. Achary, A.K. Tyagi, C. Popescu, Pressure impact on the stability and distortion of the crystal structure of $CeScO_3$, Inorg. Chem. 56 (2017) 8363–8371, https://doi.org/10.1021/acs.inorgchem.7b01042.

[18] K. Ueda, T. Aoki, Y. Shimizu, F. Massuyeau, S. Jobic, Luminescence and location of Gd^{3+} or Tb^{3+} ions in perovskite-type $LaScO_3$, Inorg. Chem. 57 (2018) 8718–8721, https://doi.org/10.1021/acs.inorgchem.8b01288.

[19] B. Veličkov, V. Kahlenberg, R. Bertram, M. Bernhagen, Crystal chemistry of $GdScO_3$, $DyScO_3$, $SmScO_3$ and $NdScO_3$, Zeitschrift Fur Kristallographie 222 (2007) 466–473, https://doi.org/10.1524/zkri.2007.222.9.466.

[20] T.M. Gesing, R. Uecker, J.C. Buhl, Refinement of the crystal structure of praseodymium orthoscandate, $PrScO_3$, Zeitschrift Fur Kristallographie - New Crystal Structures 224 (2009) 365–366, https://doi.org/10.1524/ncrs.2009.0159.

[21] R.P. Liferovich, R.H. Mitchell, A structural study of ternary lanthanide orthoscandate perovskites, J. Solid State Chem. 177 (2004) 2188–2197, https://doi.org/10.1016/j.jssc.2004.02.025.

[22] W. Su, D. Wu, X. Li, X. Ma, J. Zhou, Z. Qian, Y. Wang, W. Liu, Z. Ge, An investigation using high-pressure synthesis of double-rare-earth oxides of ABO_3-composition, Physica B: Physics of Condensed Matter & C: atomic, Molecular and Plasma Physics Optics 139–140 (1986) 658–660, https://doi.org/10.1016/0378-4363(86)90671-6.

[23] J.B. Clark, P.W. Richter, L. DuToit, High-pressure synthesis of $YScO_3$, $HoScO_3$, $ErScO_3$, and $TmScO_3$, and a reevaluation of the lattice constants of the rare earth scandates, J. Solid State Chem. 23 (1978) 129–134, https://doi.org/10.1016/0022-4596(78)90058-0.

[24] C. Artini, G.A. Costa, M.M. Carnasciali, R. Masini, Stability field and structural properties of intra-rare earth perovskites, J. Alloys Compd. 494 (2010) 336–339, https://doi.org/10.1016/j.jallcom.2010.01.030.

[25] D. Dorosz, M. Kochanowicz, R. Valiente, A. Diego-Rucabado, F. Rodríguez, N. Siñeriz-Niembro, J.I. Espeso, M. Lesniak, P. Miluski, S. Conzendorf, J. Posseckardt, Z. Liao, G.L. Jimenez, R. Müller, M. Lorenz, A. Schwuchow, M. Leich, A. Lorenz, K. Wondraczek, M. Jäger, Pr^{3+}-doped YPO_4 nanocrystal embedded into an optical fiber, Sci. Rep. 14 (2024) 7404, https://doi.org/10.1038/s41598-024-57307-4.

[26] D. Gao, B. Chen, X. Sha, Y. Zhang, X. Chen, L. Wang, X. Zhang, J. Zhang, Y. Cao, Y. Wang, L. Li, X. Li, S. Xu, H. Yu, L. Cheng, Near infrared emissions from both high efficient quantum cutting (173%) and nearly-pure-color upconversion in NaY$(WO_4)_2$:Er^{3+}/Yb^{3+} with thermal management capability for silicon-based solar cells, Light Sci. Appl. 13 (2024) 13, https://doi.org/10.1038/s41377-023-01365-2.

[27] M. De Jong, A. Meijerink, F.T. Rabouw, Non-Poissonian photon statistics from macroscopic photon cutting materials, Nat. Commun. 8 (2017) 15537, https://doi.org/10.1038/ncomms15537.

[28] R. Kolesov, K. Xia, R. Reuter, R. Stöhr, A. Zappe, J. Meijer, P.R. Hemmer, J. Wrachtrup, Optical detection of a single rare-earth ion in a crystal, Nat. Commun. 3 (2012) 1029, https://doi.org/10.1038/ncomms2034.

[29] K. Ueda, S. Tanaka, T. Yoshino, Y. Shimizu, T. Honma, Site-selective doping and site-sensitive photoluminescence of Eu^{3+} and Tb^{3+} in perovskite-type $LaLuO_3$, Inorg. Chem. 58 (2019) 10890–10897, https://doi.org/10.1021/acs.inorgchem.9b01273.

[30] A. Siaï, K. Horchani-Naifer, P. Haro-González, M. Férid, Effect of ytterbium substitution on $LaEr_{(1-x)}Yb_xO_3$ optical properties, J. Lumin. 172 (2016) 65–70, https://doi.org/10.1016/j.jlumin.2015.11.030.

[31] H. Wei, C. Yang, Y. Wu, B. Cao, M. Lorenz, M. Grundmann, From energy harvesting to topologically insulating behavior: ABO_3-type epitaxial thin films and superlattices, J Mater Chem C Mater 8 (2020) 15575–15596, https://doi.org/10.1039/d0tc02811h.

[32] V.S. Bhadram, D. Swain, R. Dhanya, M. Polentarutti, A. Sundaresan, C. Narayana, Effect of pressure on octahedral distortions in $RCrO_3$ (R = Lu , Tb , Gd , Eu , Sm): the role of R-ion size and its implications, Mater. Res. Express 1 (2014) 026111, https://doi.org/10.1088/2053-1591/1/2/026111.

[33] V.S. Bhadram, A. Sen, J. Sunil, D. Prasad, A. Sundaresan, C. Narayana, Pressure-driven evolution of structural distortions in $RCrO_3$ perovskites : the curious case of $LaCrO_3$, Solid State Sci. 119 (2021) 106708, https://doi.org/10.1016/j.solidstatesciences.2021.106708.

[34] P. Gao, Z. Chen, T.A. Tyson, T. Wu, K.H. Ahn, Z. Liu, R. Tappero, S.B. Kim, S. W. Cheong, High-pressure structural stability of multiferroic hexagonal $RMnO_3$ (R=Y, Ho, Lu), Phys. Rev. B 83 (2011) 224113, https://doi.org/10.1103/PhysRevB.83.224113.

[35] R. Vilarinho, P. Bouvier, M. Guennou, I. Peral, M.C. Weber, P. Tavares, M. Mihalik, M. Mihalik, G. Garbarino, M. Mezouar, J. Kreisel, A. Almeida, J.A. Moreira, Crossover in the pressure evolution of elementary distortions in $RFeO_3$ perovskites and its impact on their phase transition, Phys. Rev. B 99 (2019) 064109, https://doi.org/10.1103/PhysRevB.99.064109.

[36] T. Ouahrani, F.Z. Medjdoub, S. Gueddida, Á.L. Fernandez, R. Franco, N. E. Benkhettou, M. Badawi, A. Liang, J. Gonzalez, D. Errandonea, Understanding the pressure effect on the elastic, electronic, vibrational, and bonding properties of the $CeScO_3$ perovskite, J. Phys. Chem. C 125 (2021) 107–119, https://doi.org/10.1021/acs.jpcc.0c08641.

[37] N. Bura, V. Srihari, A. Bhoriya, D. Yadav, J. Singh, H.K. Poswal, N. Dilawar Sharma, Structural stability of orthorhombic $DyScO_3$ under extreme conditions of pressure and temperature, Phys. Rev. B 106 (2022) 024113, https://doi.org/10.1103/PhysRevB.106.024113.

[38] E. Zanardi, S. Radescu, A. Mujica, P. Rodríguez-Hernández, A. Muñoz, Ab initio theoretical study of $DyScO_3$ at high pressure, Crystals 13 (2023) 165, https://doi.org/10.3390/cryst13020165.

[39] Z. Sun, R. Liu, T. Zhou, X. Tang, R.J. Xie, Explore broadband near-infrared phosphor-perovskite $LaLuO_3$:Cr^{3+}, in: 19th International Conference on Optical Communications and Networks (ICOCN), IEEE, 2021, pp. 1–3, https://doi.org/10.1109/icocn53177.2021.9563659.

[40] A.A. Coelho, TOPAS and TOPAS-Academic: an optimization program integrating computer algebra and crystallographic objects written in C++, J. Appl. Crystallogr. 51 (2018) 210–218, https://doi.org/10.1107/S1600576718000183.

[41] P. Hohenberg, W. Kohn, Inhomogeneous Electron Gas, Phys. Rev. 136 (1964) B864–B871. https://doi.org/10.1103/PhysRev.136.B864.

[42] P.E. Blöchl, Projector augmented-wave method, Phys. Rev. B 50 (1994) 17953–17979, https://doi.org/10.1103/PhysRevB.50.17953.

[43] J.P. Perdew, A. Ruzsinszky, G.I. Csonka, O.A. Vydrov, G.E. Scuseria, L. A. Constantin, X. Zhou, K. Burke, Restoring the density-gradient expansion for exchange in solids and surfaces, Phys. Rev. Lett. 100 (2008) 136406, https://doi.org/10.1103/PhysRevLett.100.136406.

[44] A. Togo, L. Chaput, T. Tadano, I. Tanaka, Implementation strategies in phonopy and phono3py, J. Phys. Condens. Matter 35 (2023) 353001, https://doi.org/10.1088/1361-648X/acd831.

[45] A. Togo, First-principles phonon calculations with phonopy and Phono3py, J Physical Soc Japan 92 (2023) 012001, https://doi.org/10.7566/JPSJ.92.012001.

[46] R. Uecker, R. Bertram, M. Brützam, Z. Galazka, T.M. Gesing, C. Guguschev, D. Klimm, M. Klupsch, A. Kwasniewski, D.G. Schlom, Large-lattice-parameter perovskite single-crystal substrates, J. Cryst. Growth 457 (2017) 137–142, https://doi.org/10.1016/j.jcrysgro.2016.03.014.

[47] Y. Zhao, D.J. Weidner, J.B. Parise, D.E. Cox, Thermal expansion and structural distortion of perovskite - data for $NaMgF_3$ perovskite. Part I, Phys. Earth Planet. In. 76 (1993) 1–16, https://doi.org/10.1016/0031-9201(93)90051-A.

[48] R.H. Mitchell, Perovskites: Modern and Ancient, Almaz Press, 2002.

[49] M. Bharathy, A.H. Fox, S.J. Mugavero, H.C. zur Loye, Crystal growth of inter-lanthanide $LaLn'O_3$ (Ln' = Y, Ho-Lu) perovskites from hydroxide fluxes, Solid State Sci. 11 (2009) 651–654, https://doi.org/10.1016/j.solidstatesciences.2008.10.005.

[50] V.M. Goldschmidt, Die Gesetze der Krystallochemie, Naturwissenschaften 14 (1926) 477–485, https://doi.org/10.1007/BF01507527.

[51] R.J.D. Tilley, Perovskites: Structure-Property Relationships, Wiley, 2016.

[52] A. Siaï, K. Horchani-Naifer, P. Haro-González, M. Férid, Effects of the preparation processes on structural, electronic, and optical properties of $LaHoO_3$, Mater. Res. Bull. 76 (2016) 179–186, https://doi.org/10.1016/j.materresbull.2015.12.019.
[53] K.E. Johnston, M.R. Mitchell, F. Blanc, P. Lightfoot, S.E. Ashbrook, Structural study of $La_{1-x}Y_xScO_3$, combining neutron diffraction, solid-state NMR, and first-principles DFT calculations, J. Phys. Chem. C 117 (2013) 2252–2265, https://doi.org/10.1021/jp310878b.
[54] V. Kahlenberg, D. Maier, B. Veličkov, Redetermination of $EuScO_3$, Acta Crystallogr Sect E Struct Rep Online 65 (2009), https://doi.org/10.1107/S1600536809001433.
[55] F.N. Sayed, R. Shukla, A.K. Tyagi, A chemical method for stabilizing a new series of solid solution $Pr_{1-x}Ce_xScO_3$ ($0.0 \leq x \leq 1.0$) systems, Dalton Trans. 44 (2015) 16929–16936, https://doi.org/10.1039/C5DT01459J.
[56] A.S. Farlenkov, A.G. Smolnikov, M.V. Ananyev, A.V. Khodimchuk, A.L. Buzlukov, A.V. Kuzmin, N.M. Porotnikova, Local disorder and water uptake in $La_{1-x}Sr_xScO_{3-\delta}$, Solid State Ionics 306 (2017) 82–88, https://doi.org/10.1016/j.ssi.2017.04.018.
[57] R.L. Moreira, A. Feteira, A. Dias, Raman and infrared spectroscopic investigations on the crystal structure and phonon modes of $LaYbO_3$ ceramics, J. Phys. Condens. Matter 17 (2005) 2775–2781, https://doi.org/10.1088/0953-8984/17/17/027.
[58] M.T. Candela, F. Aguado, J. González-Lavín, J.A. González, R. Valiente, Modification of the spectroscopic properties of Tb_2O_3 phosphor under the high-pressure phase transitions sequence, J. Alloys Compd. 859 (2021) 157899, https://doi.org/10.1016/j.jallcom.2020.157899.
[59] A. Diego-Rucabado, M.T. Candela, F. Aguado, J. González, F. Rodríguez, R. Valiente, R. Martín-Rodríguez, I. Cano, A comparative study on luminescence properties of Y_2O_3: Pr^{3+} nanocrystals prepared by different synthesis methods, Nanomaterials 10 (2020) 1574, https://doi.org/10.3390/nano10081574.
[60] J. Lucas, P. Lucas, T. Le Mercier, A. Rollat, W. Davenport, Introduction to rare earth luminescent materials, in: J. Lucas, P. Lucas, T. Le Mercier, A. Rollat, W. Davenport (Eds.), Rare Earths: Science, Technology, Production and Use, Elsevier, 2015, pp. 251–280, https://doi.org/10.1016/b978-0-444-62735-3.00014-0.
[61] A.M. Srivastava, C. Renero-Lecuna, D. Santamaría-Pérez, F. Rodríguez, R. Valiente, Pressure-induced Pr^{3+} $^3P_0$ luminescence in cubic Y_2O_3, J. Lumin. 146 (2014) 27–32, https://doi.org/10.1016/j.jlumin.2013.09.028.
[62] Y. Chen, J. Wang, C. Liu, J. Tang, X. Kuang, M. Wu, Q. Su, UV-Vis-NIR luminescence properties and energy transfer mechanism of $LiSrPO_4$:Eu^{2+}, Pr^{3+} suitable for solar spectral convertor, Opt Express 21 (2013) 3161, https://doi.org/10.1364/oe.21.003161.
[63] Y. Ohishi, T. Kanamori, T. Kitagawa, S. Takahashi, E. Snitzer and, G.H. Sigel, Pr^{3+}-doped fluoride fiber amplifier operating at 1.31 μm, Opt Lett 16 (1991) 1747, https://doi.org/10.1364/ofc.1991.pd2.
[64] J. Pisarska, M. Kuwik, W.A. Pisarski, Spectroscopic properties of inorganic glasses doped with Pr^{3+}: a comparative study, Materials 15 (2022) 767, https://doi.org/10.3390/ma15030767.
[65] H.P. Labaki, F.H. Borges, F.J. Caixeta, R.R. Gonçalves, Widely dual tunable visible and near infrared emission in Pr^{3+}-doped yttrium tantalate: Pr^{3+} concentration dependence on radiative transitions from $^3P_0$ to the $^1D_2$, J. Lumin. 236 (2021) 118073, https://doi.org/10.1016/j.jlumin.2021.118073.
[66] J. Ibáñez, J.Á. Sans, V. Cuenca-Gotor, R. Oliva, Ó. Gomis, P. Rodríguez-Hernández, A. Muñoz, U. Rodríguez-Mendoza, M. Velázquez, P. Veber, C. Popescu, F. J. Manjón, Structural and lattice-dynamical properties of Tb_2O_3 under compression: a comparative study with rare earth and related sesquioxides, Inorg. Chem. 59 (2020) 9648–9666, https://doi.org/10.1021/acs.inorgchem.0c00834.
[67] J. Yang, M. Shahid, C. Wan, Anisotropy of mechanical and thermal properties of perovskite $LaYbO_3$: first-principles calculations, Phil. Mag. 98 (2018) 2917–2929, https://doi.org/10.1080/14786435.2018.1511924.